1   **ATPase and protease domain movements in the bacterial AAA+ protease**

2   **FtsH are driven by thermal fluctuations**

3

4   **Running title: Inter-domain dynamics of FtsH**

5

6   Martine Ruer[1,2,†], Georg Krainer[1,3,†], Philip Gröger[1], Michael Schlierf[1,*]

7

8   [1] B CUBE – Center for Molecular Bioengineering, Technische Universität Dresden,

9   Arnoldstr. 18, 01307 Dresden, Germany

10   [2] Current address: Max Planck Institute of Molecular Cell Biology and Genetics (MPI-CBG),

11   Pfotenhauer Str. 108, 01307 Dresden, Germany

12   [3] Molecular Biophysics, Technische Universität Kaiserslautern (TUK), Erwin-Schrödinger-

13   Str. 13, 67663 Kaiserslautern, Germany

14

15   [†] These authors contributed equally to this work.

16   [*] Corresponding author. Tel: +49 351 463 43050; E-mail: michael.schlierf@tu-dresden.de

17 **Abstract**

18   AAA+ proteases are essential players in cellular pathways of protein degradation. Elucidating

19   their conformational behavior is key for understanding their reaction mechanism and,

20   importantly, for elaborating our understanding of mutation-induced protease deficiencies. Here,

21   we study the structural dynamics of the *Thermotoga maritima* metalloprotease FtsH (*Tm*FtsH).

22   Using a single-molecule FRET approach to monitor the real-time ATPase and protease inter-

23   domain conformational changes, we show that *Tm*FtsH—even in the absence of nucleotide—is

24   a highly dynamic protease undergoing conformational transitions between five states on the

25   second timescale. Addition of ATP does not influence the number of states nor change the

26   timescale of domain motions, but affects the state occupancy distribution leading to an inter-

27   domain compaction. These findings suggest that thermal energy, but not chemical energy,

28   provides the major driving force for conformational switching, while ATP, through a state

29   reequilibration, introduces directionality into this process. The *Tm*FtsH A359V mutation, a

30   homolog of the human pathogenic A510V mutation of paraplegin causing hereditary spastic

31   paraplegia (HSP), impairs the ATP-coupled domain compaction and, thus, may account for

32   protease malfunctioning and pathogenesis in HSP.

33

Introduction

37 Cellular organisms maintain a stable and functional proteome by fine-tuned homeostasis
38 mechanisms that regulate the expression, folding, and degradation of proteins [1]. Key players
39 in the cellular pathways of protein degradation are AAA+ (ATPases associated with diverse
40 cellular activities) proteases [2,3]. These energy-dependent molecular machines remove
41 dysfunctional, misfolded, aggregated as well as no longer needed proteins from the proteome
42 by their specific unfoldase and peptidase activities [4–9]. The importance of this cellular
43 clearance system is eminently reflected in its impairments, as alterations in AAA+-based
44 proteolysis are associated with various dysfunctions in bacteria [10,11] as well as a broad range
45 of neurodegenerative, metabolic, and cancerous diseases in humans [12–16], most frequently
46 caused only by single point mutations in the protease sequence.

47 One of the prototypic and highly conserved AAA+ proteases in eubacteria, mitochondria, and
48 chloroplasts is the membrane-embedded metalloprotease FtsH [10,11,17]. FtsH forms ring-like
49 hexameric assemblies of monomer subunits exposing a central pore, through which the
50 unfolded protein substrate is translocated. Each monomeric subunit consists of a protease and
51 ATPase domain, which are connected via a hinge region [10]. Recent crystallographic
52 structures of *Thermotoga maritima* FtsH (*Tm*FtsH) without nucleotide and in the presence of
53 ADP revealed a large conformational change between the ATPase and the protease domain
54 upon ADP binding, thus suggesting an ATP-coupled chemo-mechanical cycle that involves a
55 coordinated opening and closing of the two domains between two states [18,19] (Fig. 1a). Even
56 though these structures showcase the large conformational transitions *Tm*FtsH domains can
57 undergo, mechanistic models inferred from the crystal structures often report only on a limited
58 number of conformational states and do not provide dynamic information. Elucidating the
59 underlying reaction mechanism of *Tm*FtsH and other proteases, however, requires kinetic
60 insights for understanding the interplay of ATP binding to conformational changes and,
61 importantly, for elaborating our understanding in protease deficiency-related diseases. For
62 example, the pathogenic mutation A510V of the human *Tm*FtsH-structural homolog paraplegin
63 (SPG7) can cause hereditary spastic paraplegia (HSP) [13,20–22] and is located right at the
64 hinge between the ATPase and protease domain [23], indicating that a relative movement might
65 be impaired. However, our understanding of the dynamic influence of potentially disruptive
66 mutations on conformational changes and ATP coupling remains elusive.

67 Intramolecular dynamics of multi-component enzymes like AAA+ proteases are challenging to
68 resolve because of the experimental difficulties encountered in probing the unsynchronized

69 motions of their constituent subunits or domains [24]. Recent advances in single-molecule

70 experiments have enabled the direct observation of individual molecular machines at work,

71 providing real-time kinetic information on unsynchronized nanoscale motions of enzymes and

72 their subunit structures, which have previously eluded a quantitative description by classical

73 biochemical and structural biology methods [25–29].

74 Here, we exploited a single-molecule Förster resonance energy transfer (smFRET) approach to

75 study the real-time ATPase and protease inter-domain conformational changes of *Tm*FtsH. We

76 found that inter-domain movements of monomer subunits within assembled *Tm*FtsH hexamers

77 occur on the second timescale, are thermally driven, and weakly coupled to ATP binding or

78 hydrolysis. By performing kinetic analysis based on Hidden Markov modelling, we uncovered

79 five conformational states of *Tm*FtsH, thereby expanding the previous knowledge of the two

80 crystallographic structures. Using this approach, we further studied the effects of the A359V

81 mutation, which is homologous to the human A510V paraplegin mutation, and found that this

82 mutation perturbs the conformational behavior of *Tm*FtsH upon ATP binding, thereby

83 providing a potential mechanism for protease malfunctioning and disease pathogenesis in HSP.

84 **Results**

85 **Probing the real-time conformational changes in *Tm*FtsH with smFRET**

86 To monitor ATPase and protease inter-domain dynamics in *Tm*FtsH, we established a smFRET

87 assay that allows probing of structural changes in single *Tm*FtsH monomers within self-

88 hexamerized *Tm*FtsH rings. To this end, we created a Cys-light variant (TmFtsH$_{184,513}$) lacking

89 the transmembrane domain of *Tm*FtsH (as described in Bieniossek et al. [18,19]) but carrying

90 two unique Cys residues, one at position 184 in the ATPase domain, and another wild-type

91 cysteine at position 513 in the protease domain. One fraction of TmFtsH$_{184,513}$ was kept

92 unlabeled while the other fraction was reacted with maleimide-functionalized FRET donor

93 (Cy3) and an acceptor (Cy5) fluorophores to obtain double-labeled TmFtsH$_{184,513}$ monomer

94 units (Fig. 1a). The dye labels were placed at positions close to the tip of each domain at a

95 distance such that significant changes in the FRET efficiency are expected if these domains

96 move relatively to each other. Functional assays testing the ATPase and protease activities

97 confirmed that the TmFtsH$_{184,513}$ variant retained both activities (Figs. S1 and S2, respectively).

98 To assemble TmFtsH$_{184,513}$ into their active homohexameric rings, a concentration exceeding

99 the oligomer dissociation constant on the order of ~400 nM is required. However, working with

100 such high concentrations of labeled protein in solution would result in a high background signal

101 in smFRET experiments [26]. We therefore exploited a lipid vesicle-based nanocontainer

102   approach [30] to increase the effective concentrations of *Tm*FtsH monomers through molecular

103   confinement. We encapsulated a concentrated *Tm*FtsH monomer solution in ~200-nm diameter

104   phospholipid vesicles, yielding an apparent concentration of the protease monomers inside the

105   vesicles of ~2.3 mM, thus ensuring self-hexamerization (Fig. 1b). Co-encapsulation of labeled

106   and unlabeled *Tm*FtsH$_{184,513}$ monomers in a 1:5 ratio yields one labeled *Tm*FtsH$_{184,513}$ per

107   assembled hexamer on average, thus allowing to probe conformational switching of one

108   monomer within an active homohexameric ring. The lipid vesicles were composed of 1,2-

109   dimyristoyl-*sn*-glycero-3-phosphocholine (DMPC), which selectively permeabilizes the

110   membrane for ATP addition [30], and contained also a small fraction of 1,2-dipalmitoyl-*sn*-

111   glycero-3-phosphoethanolamine-N-(cap biotinyl) (biotin-DPPE) to tether the vesicles to a

112   quartz slide via biotin–streptavidin interactions. We immobilized the preassembled and

113   *Tm*FtsH$_{184,513}$-filled vesicles on a polyethylene glycol (PEG)–biotin-coated chamber via a

114   biotin–neutravidin–biotin sandwich and performed real-time imaging of fluorescently-labeled

115   single molecules with a prism-based total internal reflection fluorescence (TIRF) microscope

116   [31,32].

117

118
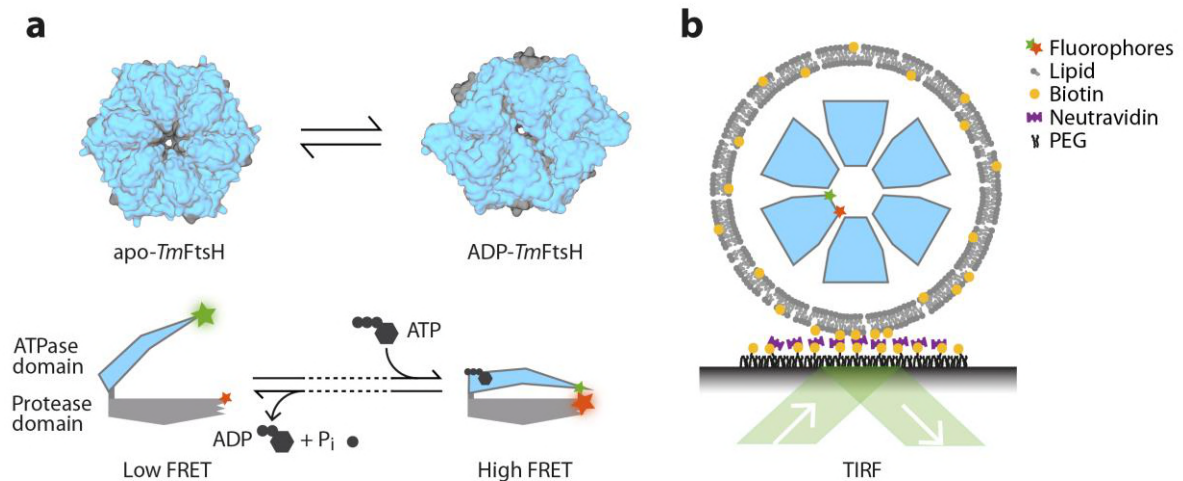
Figure 1. ATPase and protease inter-domain movements in *Tm*FtsH probed by smFRET. a) Schematics of large-scale conformational changes in *Tm*FtsH. Upper panel: surface representation of hexameric *Tm*FtsH in its apo- (left, pdb: 3kds) and ADP-bound state (right, pdb: 2cea) [18,19]. The protease and ATPase domains are colored in gray and blue, respectively. Visualization was performed in VMD [33]. Lower panel: Schematic of monomer subunit domain conformational changes between an open and a closed state upon ATP binding and hydrolysis as suggested from crystal-structure analysis of *Tm*FtsH. The positions used for labeling with donor (Cy3, green star) and acceptor fluorophores (Cy5, red star) in *Tm*FtsH$_{184,513}$ are indicated. b) Experimental

5

128 design of the smFRET assay. Double-labeled TmFtsH$_{184,513}$ monomers were self-
129 assembled in presence of unlabeled TmFtsH to hexamers in DMPC lipid vesicles
130 containing a small fraction of biotin-DPPE. Lipid vesicles were surface-immobilized via
131 a biotin–streptavidin–biotin sandwich and TmFtsH domain conformational changes were
132 monitored by smFRET TIRF microscopy.

133

134 **Apo-TmFtsH undergoes sequential transitions between five conformational states**

135 In a first set of experiments, we investigated conformational changes of TmFtsH$_{184,513}$ in the
136 absence of ATP. Donor (I_D) and acceptor (I_A) fluorescence intensities from assembled hexamers
137 in lipid vesicles were recorded for tens of seconds at ten frames per second (Fig. 2a). smFRET
138 time trajectories were extracted by calculating the apparent FRET efficiencies
139 ($E_{app} = I_A / (I_D + I_A)$) for each collected data point. Only trajectories exhibiting single bleaching
140 steps of both the donor and acceptor fluorophore were investigated to ensure that FRET
141 efficiency changes arise only from single donor–acceptor labeled monomers and not from
142 multiple co-encapsulated labeled subunits. The donor and acceptor fluorescence time traces
143 showed anti-correlated signals fluctuations between low and high intensity (Fig. 2a), which
144 translate into highly dynamic FRET efficiency changes (Fig. 2b) revealing that TmFtsH$_{184,513}$
145 exhibits inter-domain movements between the ATPase and protease domain on the second
146 timescale. Based on the structural data, we expected a constant low FRET efficiency in absence
147 of ATP, however, the large distinct changes between $E_{min} \approx 0.2$ and $E_{max} \approx 0.9$ observed in the
148 smFRET time trajectories indicate a large hinge-bending motion in the range of ~3–4 nm
149 between the two domain tips. FRET efficiency histograms from individual time traces (Fig. 2b,
150 right panel) as well as a cumulative FRET efficiency histogram from all trajectories ($n = 108$)
151 resulted in a broad distribution, further supporting that the ATPase and protease domains of
152 TmFtsH$_{184,513}$ dynamically interconvert between multiple states in absence of ATP.

153 To resolve the number of states adopted by TmFtsH$_{184,513}$ and to derive kinetic information on
154 inter-domain switching, we analyzed the obtained smFRET time trajectories by global Hidden
155 Markov modelling using ebFRET [34] (Fig. 2c). This analysis revealed that smFRET time
156 traces are best described by five distinct conformational states, as indicated by the minimum in
157 an unbiased global Bayesian Information Criterion (BIC) function (Fig. 2d). A Viterbi path
158 reconstruction of the entire set of time trajectories using a five-state model excellently
159 reproduced the experimental smFRET trajectories (Fig. 2c, left panel and Fig. S7 for more
160 example data) and allowed us to extract state dwell times and kinetic rates. A histogram created
161 from the reconstructed Viterbi paths covered the full distribution of underlying conformational

162   states (Fig. 2c, right panel), substantiating that the conformational switching of TmFtsH$_{184,513}$ is

163   well described by five dynamically interconverting states. A rate matrix (Fig. 2e) generated for

164   all closing and opening transitions revealed that transitions between neighboring states (e.g.,

165   state 1 to state 2) are much more frequently observed than transitions between other states (e.g.,

166   state 1 to state 4), indicating that conformational switching of TmFtsH$_{184,513}$ occurs primarily in

167   a sequential manner to the nearest neighbor state. A graphical representation summarizing the

168   relative occupancies and kinetic rates for opening and closing transitions between the nearest

169   neighbor states is shown in Figure 3a.

170
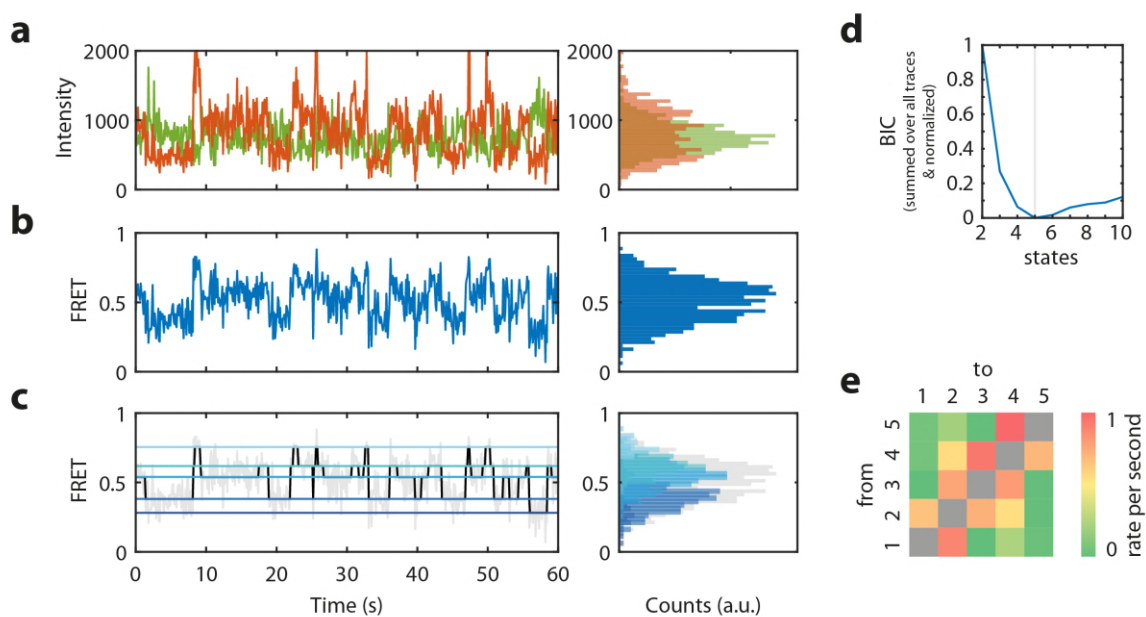
171

172   **Figure 2. Opening and closing of the TmFtsH domains in the absence of ATP.**
173   a) Representative donor and acceptor fluorescence intensity time trajectories (left panel)
174   and their distributions (right panel). b) smFRET time trajectory (left panel) constructed
175   from (a) and the derived FRET efficiency histogram (right panel) c) Viterbi path
176   reconstruction of the smFRET time trajectory in (b) using a five-state model (left panel)
177   and the derived histogram (right panel) d) Global BIC function. e) Heatmap of all
178   conformational transition rates of TmFtsH$_{184,513}$ in the absence of ATP.

179

ATP shifts the population equilibrium towards a more compacted state

181   In a next step, we wanted to test whether the presence of ATP has an influence on the

182   conformational dynamics of TmFtsH, as ATP has been inferred from crystallographic studies

183   to influence the chemo-mechanical state [19]. To this end, we performed smFRET

184   measurements on TmFtsH$_{184,513}$ in the presence of 1 mM ATP. Similar to our observations

7

185 without ATP, smFRET time trajectories showed large fluctuations between multiple states on
186 the second timescale (Figs. S4a,b and S7b for more example data). A FRET efficiency
187 histogram created from all trajectories exhibits a broad distribution, indicating again a large
188 opening and closing motion of both domains ranging from $E_{min} \approx 0.3$ to $E_{max} \approx 0.9$ (Fig. S4b).
189 Interestingly, the FRET efficiency distribution is skewed to slightly higher FRET efficiencies
190 compared to TmFtsH$_{184,513}$ in the absence of ATP. This indicates that TmFtsH assumes a more
191 compact conformation when ATP is present. To shed light on whether this apparent shift is
192 caused by a repopulation of FRET states or a shift of FRET states towards higher FRET
193 efficiencies, we analyzed the time trajectories using Hidden Markov modelling ($n = 17$
194 trajectories). As seen for the experiments without ATP, we found conformational transitions
195 between five states indicated by the minimum in the BIC function (Fig. S4d). Moreover,
196 transitions also occurred most frequently between direct neighboring conformational states,
197 which exhibited the highest transition rates (Fig. S4e). The FRET efficiency states in the
198 absence and presence of ATP agree well within error, indicating that similar molecular states
199 are adopted under both conditions (Fig. S4c). However, we observed state population
200 probabilities shifting to a higher population of state 3 as compared to the absence of ATP
201 (Fig. 3b). Thus, while the timescale of interstate conversion is similar, the equilibrium of states
202 is shifted. A higher closing-to-opening ratio between states 1 and 2 and state 2 and 3 in the
203 presence of ATP leads to a depopulation of state 1 and, thus, an increased net probability of the
204 third conformational state. In total, TmFtsH$_{184,513}$ spent 37% of its time in state 3 in the presence
205 of ATP compared to 28% in absence of ATP. Interestingly, the kinetic ratios between state 3
206 and 4 and state 4 and 5 are similar although absolute numbers vary, thus indicating that ATP
207 does not affect the equilibrium of these transitions to a great extent. Furthermore, we observed
208 that populating state 1 in presence of ATP occurred only in rare cases leading to a 7% occupancy
209 probability (vs. 17% FRET state population without ATP). Taken together, the re-equilibrations
210 explain the overall shift of the open conformational states 1 and 2 towards a more compact
211 conformation in state 3 in the presence of ATP.

212
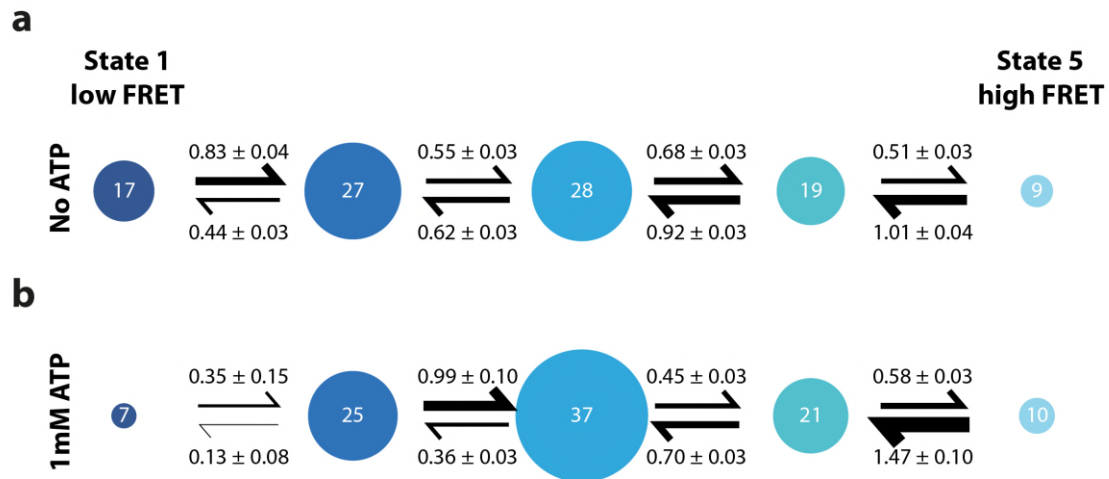
Figure 3. TmFtsH$_{184,513}$ sequential conformational switching without and with ATP.
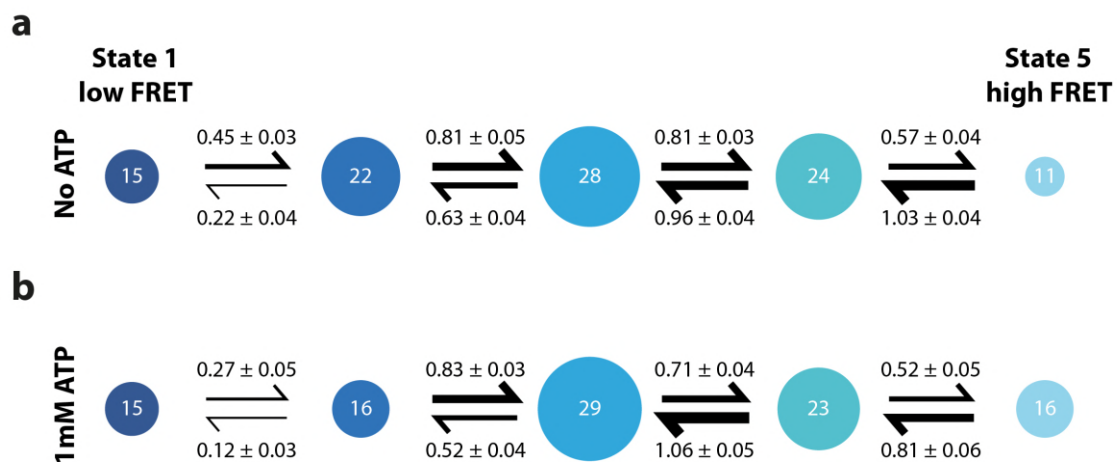Occupancies (%) and kinetic rates (per second) of TmFtsH$_{184,513}$ without (a) and with 1 mM ATP (b). Size of states and thickness of arrows scale with the occupancy probabilities and kinetic rates, respectively. State occupancies showed an error <3%.

A pathogenic mutation of the human homolog paraplegin hinders TmFtsH compaction

The human homolog of TmFtsH, paraplegin (SPG7), shares 53% structural identity and >70% similarity with TmFtsH [23] (Fig. S3). The pathogenic mutation of paraplegin A510V is associated with the autosomal recessive form of HSP, causing progressive spastic paralysis in the lower limbs [20]. Yet, its molecular effects remain elusive. A510V is highly conserved and located at the hinge interface between the ATPase and protease domains, however, it is far from both active sites [23] and still impairs the function of paraplegin [35]. Hence, we wanted to address if the malfunction caused by the mutation of the TmFtsH-homolog arises from a structural or dynamic deficiency. To this end, we introduced the paraplegin A510V-homologous mutation A359V in TmFtsH$_{184,513}$ and created fluorescently labeled mutant protein, thereafter named TmFtsH$_{184,513}$-A359V. In functional assays, the A359V mutation did not alter ATPase and protease activities compared to TmFtsH$_{184,513}$ (Figs. S1 and S2, respectively). We hexamerized TmFtsH$_{184,513}$-A359V in lipid vesicles and performed smFRET measurements both in the absence and presence of ATP. smFRET time trajectories showed similar transitions between multiple discrete states as observed for TmFtsH$_{184,513}$, revealing that the highly dynamic switching between multiple states on the second timescale is preserved in TmFtsH$_{184,513}$-A359V (Figs. S5a,b, S6a,b). The dynamic behavior resulted also in broad distributions in the cumulative smFRET efficiency histograms ranging between $E_{min} = 0.2$ and $E_{max} = 0.9$ (Figs. S5b, S6b). We analyzed all smFRET trajectories using Hidden Markov

238   modelling, which revealed five conformational states as observed for TmFtsH$_{184,513}$, both in the

239   absence and presence of ATP (Figs. S5c, S6c, S7c,d) and with a preferential switching between

240   neighboring states (Figs. S5d, S6d). In the absence of ATP, the overall state occupancy

241   distribution of TmFtsH$_{184,513}$-A359V is largely unaffected by the point mutation (Fig. 4a) when

242   compared to TmFtsH$_{184,513}$. However, a different behavior between TmFtsH$_{184,513}$-A359V and

243   TmFtsH$_{184,513}$ is observed in the presence of ATP (Fig. 4b). While TmFtsH$_{184,513}$-A359V also

244   undergoes switching on the second timescale, ATP does not induce the overall compaction of

245   TmFtsH towards the conformational state 3 as observed in TmFtsH$_{184,513}$ (c.f. Fig. 3b). Instead,

246   the equilibria between states 1 to 3 were largely unchanged in presence of ATP. This suggests

247   that the conformational switch towards a more closed conformational state in presence of ATP

248   is inhibited in mutant TmFtsH$_{184,513}$-A359V.

249

251   **Figure 4. TmFtsH$_{184,513}$-A359V sequential conformational switching without and**
252   **with 1 mM ATP.** Occupancies (%) and kinetic rates (per second) of TmFtsH$_{184,513}$-
253   A359V without (a) and with 1 mM ATP (b). Size of states and thickness of arrows scale
254   with the occupancy probability and kinetic rate, respectively. State occupancies showed
255   an error <3%.

256

Discussion

258   Resolving the inter-domain conformational changes of TmFtsH is an essential step towards

259   elucidating its proteolysis mechanism. Previous crystallographic studies on TmFtsH indicated

260   that binding of ADP drives a large conformational transition from an open state in the apo form

261   to a closed state, in which the ATPase domain is closely associated with the protease domain

262   [10,18,19]. A model of the chemo-mechanical cycle was inferred from these two crystal

10

263 structures, describing *Tm*FtsH's function with a power-stroke mechanism, whereby the energy

264 released by ATP hydrolysis is converted into a conformational switch. While these structures

265 granted Ångström-resolved snapshots of two distinct conformers of the protease, they did not

266 reveal the connectivity between the states nor provided time trajectories of structural changes

267 and their coupling to ATP binding.

268 In this work, we established a kinetic view on *Tm*FtsH's ATPase and protease inter-domain

269 switch by using time-resolved smFRET to monitor the unsynchronized domain movements of

270 *Tm*FtsH monomers within self-assembled hexamers. We found that *Tm*FtsH is a highly

271 dynamic protease, even in the absence of nucleotide, and undergoes sequential, thermally-

272 driven closing and opening motions through five discrete conformational states with an

273 occupancy on the second timescale. The observed amplitude of the conformational switch

274 between the two domain tips spans a length scale of ~3–4 nm and is thus consistent with the

275 large-scale hinge-bending motion seen in the crystal structures. Yet, the three additional

276 conformational states, as witnessed by our single-molecule time trace analysis, indicate a much

277 more complex structural reorganization than implied by the two-state picture inferred from the

278 crystallographic snapshots.

279 In the presence of ATP, *Tm*FtsH also performs highly dynamic switching between five different

280 states on the second timescale but the protease undergoes an inter-domain compaction caused

281 by a depopulation of the open state towards a more closed state. While compaction is in line

282 with the closing action implied by the model derived from the crystal structure upon ADP

283 binding, the thermally driven and, thus, weakly ATP-coupled inter-domain movement behavior

284 markedly differs from the existing conformational model, in which dynamic switching of

285 *Tm*FtsH was described to be purely driven by energy conversion from ATP. Our kinetic data

286 rather suggest a model (Fig. 5a) in which thermal energy, but not chemical energy derived from

287 ATP, provides the major driving force of the conformational fluctuations, while ATP, through

288 a state reequilibration, introduces directionality into these thermal domain motions. Support for

289 a weakly ATP-coupled inter-domain reconfiguration model comes from a comparison of

290 *Tm*FtsH's ATP consumption rates and its conformational transition rates. The ATPase activity

291 of *Tm*FtsH$_{184,513}$ with 7×10^{-4} ATP/monomer/s is significantly slower than the second timescale

292 inter-domain conformational dynamics observed in our smFRET experiments, both without and

293 with ATP, thus substantiating the notion that ATP itself might not be an important driver in

294 conformational changes of *Tm*FtsH in its chemo-mechanical cycle.

11

295   A largely energy-independent or weakly ATP-coupled conformational switching mechanism

296   resembles previous work on the dimeric ATPase chaperone Hsp90 [36], where conformational

297   changes between different states of the protein were found to result from thermal fluctuations

298   rather than from the release of chemical energy upon ATP hydrolysis. Low lying energy barriers

299   on the order of a few k_bTs together with multiple discrete conformational states were suggested

300   to drive the conformational changes sequentially in Hsp90. Such a mechanism might also be at

301   play in *Tm*FtsH and explain how thermal fluctuations are sufficient for *Tm*FtsH to drive

302   sequential transitions from one state to a neighbor state, thus not necessitating ATP energy

303   conversion for its domain fluctuations.

304   From a functional point of view, the mechanism of thermally-induced conformational switching

305   in *Tm*FtsH may be of importance for its unfoldase or translocase activity. By severing the large

306   conformational switching into small transitions, the partial thermally-unfolded protein substrate

307   bound at the ATPase domain of *Tm*FtsH could be transferred to the proteolytic domain, similar

308   to previous reports of thermal ratchets [37,38], while ATP might aid in establishing

309   directionality in this process. Even though conformational switching appears largely

310   independent of energy use, we speculate that ATP hydrolysis might be required for unfolding

311   of mechanically stable substrates, as recently observed for the bacterial ClpXP system and I27

312   as well as green fluorescent protein (GFP) unfolding [6,8,39–41].

313
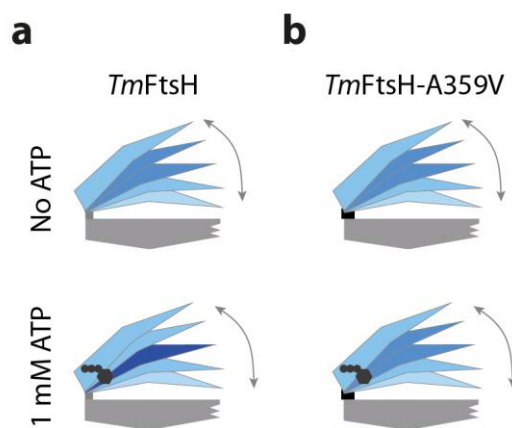
314

315   **Figure 5. Model of thermally-driven domain motions in *Tm*FtsH and the effect of**
316   **hindered movement upon introduction of a pathological hinge point mutation.**
317   a) *Tm*FtsH and b) *Tm*FtsH-A359V without ATP (upper panel) and with 1 mM ATP
318   (bottom panel). Blue scaling of the ATPase domain indicates occupancies of the
319   conformational state, with a darker color indicating a higher occupied state.

320

12

321   The thermally-driven domain motions in *Tm*FtsH suggest an important role of the hinge

322   interface connecting the ATPase and protease domain in mediating the conformational switch,

323   which might be disturbed when mutations are introduced. To address this question, we studied

324   the conformational dynamics of *Tm*FtsH carrying the A359V mutation, a hinge point mutation

325   which is homologous to the HSP-pathogenic mutation of paraplegin A510V [20,23]. We found

326   that *Tm*FtsH-A359V also performs switching between five different conformational states with

327   thermally driven interconversion on the seconds timescale. However, *Tm*FtsH-A359V did not

328   show the characteristic compaction towards state 3 upon addition of ATP as seen in *Tm*FtsH,

329   but exhibited, within error, unchanged population occupancies of its five states. With 4×10^{-4}

330   ATP/hexamer/s, the point mutation itself did not significantly alter the ATPase activity of

331   *Tm*FtsH$_{184,513}$-A359V. Thus, we speculate that the mutation A359V might hinder an allosteric

332   communication upon ATP binding or hydrolysis as the molecule is 'locked' in a more open

333   state than could be evoked by ATP binding or hydrolysis. We anticipate that this hindered

334   communication could also be the molecular cause of the malfunction in the human paraplegin

335   A510V mutation (Fig. 5b).

336   Whereas the presence of substrate stimulates ATP hydrolysis (Fig. S1), it remains unknown if

337   substrate binding would change the occupancies of the molecular conformations or the dynamic

338   behavior of domain motions and their ATP coupling behavior. Further smFRET experiments

339   using different protease substrates with both *Tm*FtsH and *Tm*FtsH-A359V should shed light on

340   the existence of a substrate-induced energy-coupled mechanism of degradation and potentially

341   further malfunctions of pathogenic mutations. Noteworthy, our results, together with earlier

342   work that reported ATP-independent proteolytic activity of *Tm*FtsH—which we also observed

343   with the weakly folded protein substrate casein for *Tm*FtsH$_{184,513}$ (Fig. S2)—indicate the

344   possibility that the proteolytic activity could be decoupled from ATPase activity. Thus, it

345   remains to be explored how *Tm*FtsH could use a dual mechanism for processing its protein

346   substrates: one ATP dependent and one ATP independent.

347   In conclusion, we found that conformational changes between the ATPase and the protease

348   domain of *Tm*FtsH are driven by thermal motions and only weakly coupled to ATP. *Tm*FtsH

349   adopts five discrete, well-defined states during closing and opening cycles, which remain to be

350   structurally resolved. The presence of ATP favors compaction of *Tm*FtsH with higher

351   occupancy of state 3 along the closing cycle, yet all five conformational states are frequently

352   adopted by *Tm*FtsH. Introducing a mutation in the hinge interface of *Tm*FtsH, homologous to a

353   human pathogenic mutation of paraplegin causing HSP, prevents the compaction observed by

13

354 the ATPase and protease domains of *Tm*FtsH, a perturbation that might explain the pathogenic

355 activity of the human homolog paraplegin causing HSP.

356 **Materials and Methods**

357 **Protein design, production, and purification.** The cDNA sequence corresponding to amino

358 acid residues 147–610 of *Tm*FtsH was inserted between the NcoI and NotI sites of a pET28a(+)

359 vector (Novagen) to encode an N-terminal His$_6$-tagged *Tm*FtsH fusion protein lacking the

360 transmembrane domain (Δtm) of *Tm*FtsH (His$_6$-(Δtm)*Tm*FtsH(147–610)), as described in

361 Bieniossek et al. [18,19]. A plasmid encoding a double Cys variant (*Tm*FtsH$_{184,513}$) of His$_6$-

362 (Δtm)*Tm*FtsH(147–610) for site-specific labeling with thiol-reactive fluorophores at positions

363 184 and 513 was created by introducing a non-native Cys at position 184 and by replacing the

364 two native Cys residues at positions 255 and 564 by Ser residues to prevent unspecific labeling.

365 The expression vector encoding the mutant *Tm*FtsH$_{184,513}$-A359V variant was generated from

366 the *Tm*FtsH$_{184,513}$ plasmid by an Ala-to-Val replacement at position 359. Mutations were

367 introduced using the QuikChange Lightning Multi site-directed mutagenesis kit (Novagen).

368 Target mutations in all constructs were confirmed by DNA sequencing.

369 Recombinant production of *Tm*FtsH$_{184,513}$ and *Tm*FtsH$_{184,513}$-A359V fusion proteins was

370 performed using the *Escherichia coli* host strain BL21(DE3) (Novagen). Briefly, bacterial cells

371 were transformed with the respective *Tm*FtsH$_{184,513}$- or *Tm*FtsH$_{184,513}$-A359V-encoding

372 pET28a(+) expression vector and grown in Luria-Bertani medium (supplemented with

373 50 µg/ml Kanamycin) to an optical density at 600 nm (OD$_{600}$) of ~0.6. Expression was induced

374 by the addition of isopropyl-*β*-D-1-thiogalactopyranoside (IPTG) to a final concentration of

375 0.5 mM and cells cultivated for a further 3 h at 37°C. Cells were harvested by centrifugation

376 and lysed using an Emulsiflex high-pressure homogenizer (Avestin). The soluble crude extract

377 was then separated from the cell debris and insoluble content by centrifugation for 40 min at

378 40,000 rpm at 4°C. The supernatant was subjected to heat purification at 75°C for 3 min,

379 followed by subsequent centrifugation for 10 min at 40,000 rpm and 4°C, according to

380 previously published procedures [18,19].

381 Protein purification was performed via immobilized-metal-ion affinity chromatography

382 (IMAC). Briefly, the soluble fraction of the cell lysate was applied to a HisTrap FastFlow

383 column (GE Healthcare) that had been pre-equilibrated with binding buffer (20 mM HEPES

384 pH 8.0, 300 mM NaCl, 10 mM imidazole). After extensive washing with washing buffer

385 (20 mM HEPES pH 7.5, 300 mM NaCl, 40 mM imidazole), his-tagged proteins were eluted

386 with elution buffer (20 mM HEPES pH 7.5, 300 mM NaCl, 250 mM imidazole).

387 **ATPase and protease activity assays.** ATPase activities of TmFtsH$_{184,513}$ and TmFtsH$_{184,513}$-
388 A359V were tested using the EnzChek Phosphate Assay kit (Thermo Fisher) according to the
389 manufacturer's instructions. Absorption was monitored at 360 nm (Fig. S1) after successively
390 adding ATP (1 mM), cI–ssrA substrate (0.8 µM) and TmFtsH$_{184,513}$ (14.4 µM) or TmFtsH$_{184,513}$-
391 A359V (14.4 µM) to the blank buffer solution containing 20 mM HEPES pH 8.0, 150 mM KCl,
392 10% glycerol, 5 mM MgOAc, 12.5 µM ZnOAc. The cI–ssrA substrate, an N-terminal His$_6$-
393 tagged and C-terminal ssrA-tagged (AANDENYALAA) repressor protein cI fusion protein,
394 was recombinantly produced in *E. coli* from a pET28(+) vector and purified by IMAC, followed
395 by dialysis against buffer (20 mM HEPES pH 8.0, 150 mM KCl, 10% glycerol).

396 Protease activity tests of TmFtsH$_{184,513}$ and TmFtsH$_{184,513}$-A359V were carried out by incubating
397 2.4 µM protease sample with various combinations of 1 mM casein, 1 mM ATP and 1 mM
398 EDTA overnight at 24°C and 50°C in buffer containing 20 mM HEPES pH 8.0, 150 mM KCl,
399 10% glycerol, 5 mM MgOAc, 12.5 µM ZnOAc. Protease activity was monitored by substrate
400 degradation using sodium dodecyl sulfate polyacrylamide gel electrophoresis (SDS-PAGE)
401 (Fig. S2). Casein stock solution (0.65% (*w/v*)) was prepared by dissolving bovine casein
402 (Sigma) in buffer containing 50 mM HEPES pH 8.0.

403 **Protein labeling.** TmFtsH$_{184,513}$ and TmFtsH$_{184,513}$-A359V were labeled with maleimide-
404 functionalized sulfo-Cy3 and sulfo-Cy5 dyes (both from GE Healthcare). Purified TmFtsH$_{184,513}$
405 or TmFtsH$_{184,513}$-A359V at a final concentration of 20 µM were reacted with a 10–15-fold
406 excess of both dyes under reducing conditions (0.4 mM tris(2-carboxyethyl)phosphine (TCEP))
407 in buffer containing 20 mM HEPES pH 7.5, 300 mM NaCl, 250 mM imidazole. The labeling
408 reaction was carried out for 2 h at room temperature, followed by overnight incubation at 4°C.
409 Labeled protein was separated from the unreacted dyes by IMAC using a spin-column
410 purification protocol. Briefly, after diluting the labeling reaction tenfold in binding buffer
411 (20 mM HEPES pH 8.0, 300 mM NaCl, 10 mM imidazole), the solution was applied to a Ni-
412 NTA Agarose resin (Thermo Fisher) that had been pre-equilibrated with binding buffer. After,
413 extensive spin-washing at 2,000 rpm with binding buffer until the supernatant was clear and
414 free of residual dyes, the labeled protein was eluted with elution buffer (20 mM HEPES pH 8.0,
415 300 mM NaCl, 250 mM imidazole) by centrifugation for 2 min at 2,000 rpm. Labeling
416 efficiency was determined photometrically.

417 **Sample preparation for single-molecule FRET experiments.** DMPC and biotin-DPPE lipid
418 powders (both from Avanti Polar Lipids) were dissolved in chloroform and mixed in a 99:1
419 DMPC:biotin-DPPE ratio at a final concentration of 5 mg/ml. Solvent was subsequently

420 removed by vacuum drying overnight to yield a dried lipid cake. In a separate step, labeled

421 TmFtsH$_{184,513}$ was mixed with unlabeled TmFtsH$_{184,513}$ in a 1:5 ratio at a final protein

422 concentration of 12 µM in buffer (20 mM HEPES pH 8.0, 150 mM KCl, 10% glycerol, 5 mM

423 MgOAc, 12.5 µM ZnOAc) using labeled and unlabeled protein from the same purification

424 batch. The protein mix was then added to the dried lipid cake and incubated at 37°C for 30 min.

425 After addition of additional buffer (20 mM HEPES pH 8.0, 150 mM KCl, 10% glycerol, 5 mM

426 MgOAc, 12.5 µM ZnOAc), protein encapsulation into unilamellar lipid vesicles was performed

427 by 35-fold extrusion of the protein–lipid suspension through polycarbonate filters with a pore

428 diameter of 200 nm using a Mini-Extruder (Avanti Polar Lipids) at 37°C according to the

429 manufacturer's instructions. TmFtsH$_{184,513}$-loaded vesicles were then immobilized on a

430 biotinylated PEG-coated flow chamber via a biotin–neutravidin–biotin sandwich. Before

431 single-molecule imaging, the sample chamber was supplemented with imaging buffer (20 mM

432 HEPES pH 8.0, 100 mM NaCl, 5 mM MgOAc, 12.5 µM ZnOAc) containing saturated, aged

433 Trolox (6-hydroxy-2,5,7,8-tetramethylchroman-2-carboxylic acid, Sigma) and an oxygen

434 scavenging system (100 µg/ml glucose oxidase, 0.8% (w/v) D-glucose, and 1 µU/ml catalase).

435 For measurements in the presence of ATP, 1 mM ATP was added to the imaging buffer

436 solution. Because the transition temperature of DMPC is at room temperature (~24°C)—the

437 temperature at which our experiments were performed—coexistence of liquid and gel phases

438 of the lipids permeabilizes the membrane for exchanging small molecules such as ATP [30].

439 Sample preparation for experiments with TmFtsH$_{184,513}$-A359V was carried out in the same

440 way.

441 **Single-molecule FRET experiments.** A custom-built prism-type TIRF microscope was used

442 for single-molecule data acquisition as previously described [31,32,42]. Imaging was

443 performed at room temperature. Single-molecules donor and acceptor intensities (I_D, I_A) were

444 recorded over time at 100-ms time resolution and smFRET time trajectories were extracted by

445 calculating E_{app} for each collected data point (see Results). Distances (r) were approximated on

446 the basis of the Förster equation, $r = R_0 \times (1/(E - 1))^{1/6}$, where E is the corrected FRET

447 efficiency, and R_0 is the Förster distance of the Cy3/Cy5 FRET pair ($R_0 = 5$ nm), with the

448 assumption that the fluorophores can freely rotate at the labeling site. Only traces that exhibited

449 single donor and acceptor bleaching steps were evaluated. Hidden-Markov model analysis was

450 performed using ebFRET as described [34] (https://ebfret.github.io).

16

Author contributions

MS and MR conceived experiments, MR performed experiments, PG provided analytical tools; all authors analyzed and interpreted data; MR, GK and MS wrote the manuscript; all authors discussed results and commented on the manuscript.

Conflict of interest

The authors declare no conflict of interest.

References

1. Morimoto RI, Selkoe DJ, Kelly JW (2012) *Protein homeostasis*. Cold Spring Harbor Laboratory Press, Cold Spring Harbor.

2. Sauer RT, Baker TA (2011) AAA+ proteases: ATP-fueled machines of protein destruction. *Annu Rev Biochem* **80**: 587–612.

3. Gerdes F, Tatsuta T, Langer T (2012) Mitochondrial AAA proteases — Towards a molecular understanding of membrane-bound proteolytic machines. *Biochim Biophys Acta - Mol Cell Res* **1823**: 49–55.

4. Hanson PI, Whiteheart SW (2005) AAA+ proteins: have engine, will work. *Nat Rev Mol Cell Biol* **6**: 519–529.

5. White SR, Lauring B (2007) AAA+ ATPases: achieving diversity of function with conserved machinery. *Traffic* **8**: 1657–1667.

6. Cordova JC, Olivares AO, Shin Y, Stinson BM, Calmat S, Schmitz KR, Aubin-Tam M-E, Baker TA, Lang MJ, Sauer RT (2014) Stochastic but highly coordinated protein unfolding and translocation by the ClpXP proteolytic machine. *Cell* **158**: 647–658.

7. Olivares AO, Kotamarthi HC, Stein BJ, Sauer RT, Baker TA (2017) Effect of directional pulling on mechanical protein degradation by ATP-dependent proteolytic machines. *Proc Natl Acad Sci U S A* **114**: E6306–E6313.

481   8.   Yang Y, Guo R, Gaffney K, Kim M, Muhammednazaar S, Tian W, Wang B, Liang J,
482   Hong H (2018) Folding-Degradation Relationship of a Membrane Protein Mediated by
483   the Universally Conserved ATP-Dependent Protease FtsH. *J Am Chem Soc* **140**: 4656–
484   4665.

485   9.   Neuwald AF, Aravind L, Spouge JL, Koonin E V. (1999) AAA+: A class of
486   chaperone-like ATPases associated with the assembly, operation, and disassembly of
487   protein complexes. *Genome Res* **9**: 27–43.

488   10. Langklotz S, Baumann U, Narberhaus F (2012) Structure and function of the bacterial
489   AAA protease FtsH. *Biochim Biophys Acta* **1823**: 40–48.

490   11. Ito K, Akiyama Y (2005) Cellular functions, mechanism of action, and regulation of
491   FtsH protease. *Annu Rev Microbiol* **59**: 211–231.

492   12. Turk B (2006) Targeting proteases: successes, failures and future prospects. *Nat Rev
493   Drug Discov* **5**: 785–799.

494   13. Rugarli EI, Langer T (2012) Mitochondrial quality control: a matter of life and death
495   for neurons. *EMBO J* **31**: 1336–1349.

496   14. Bulteau A-L, Bayot A (2011) Mitochondrial proteases and cancer. *Biochim Biophys
497   Acta* **1807**: 595–601.

498   15. Levytskyy RM, Germany EM, Khalimonchuk O (2016) Mitochondrial Quality Control
499   Proteases in Neuronal Welfare. *J Neuroimmune Pharmacol* **11**: 629–644.

500   16. Rugarli EI, Langer T (2006) Translating m-AAA protease function in mitochondria to
501   hereditary spastic paraplegia. *Trends Mol Med* **12**: 262–269.

502   17. Licht S, Lee I (2008) Resolving individual steps in the operation of ATP-dependent
503   proteolytic molecular machines: from conformational changes to substrate translocation
504   and processivity. *Biochemistry* **47**: 3595–3605.

505   18. Bieniossek C, Schalch T, Bumann M, Meister M, Meier R, Baumann U (2006) The
506   molecular architecture of the metalloprotease FtsH. *Proc Natl Acad Sci U S A* **103**:
507   3066–3071.

508   19. Bieniossek C, Niederhauser B, Baumann UM (2009) The crystal structure of apo-FtsH
509   reveals domain movements necessary for substrate unfolding and translocation. *Proc
510   Natl Acad Sci U S A* **106**: 21579–21584.

511   20. Sánchez-Ferrero E, Coto E, Beetz C, Gámez J, Corao AI, Díaz M, Esteban J, del

512   Castillo E, Moris G, Infante J, et al. (2013) SPG7 mutational screening in spastic
513   paraplegia patients supports a dominant effect for some mutations and a pathogenic
514   role for p.A510V. *Clin Genet* **83**: 257–262.

515 21. Roxburgh RH, Marquis-Nicholson R, Ashton F, George AM, Lea RA, Eccles D,
516   Mossman S, Bird T, van Gassen KL, Kamsteeg E-J, et al. (2013) The p.Ala510Val
517   mutation in the SPG7 (paraplegin) gene is the most common mutation causing adult
518   onset neurogenetic disease in patients of British ancestry. *J Neurol* **260**: 1286–1294.

519 22. Salinas S, Proukakis C, Crosby A, Warner TT (2008) Hereditary spastic paraplegia:
520   clinical features and pathogenetic mechanisms. *Lancet Neurol* **7**: 1127–1138.

521 23. Karlberg T, van den Berg S, Hammarström M, Sagemark J, Johansson I, Holmberg-
522   Schiavone L, Schüler H (2009) Crystal structure of the ATPase domain of the human
523   AAA+ protein paraplegin/SPG7. *PLoS One* **4**: e6975.

524 24. Bustamante CJ, Kaiser CM, Maillard RA, Goldman DH, Wilson CAM (2014)
525   Mechanisms of cellular proteostasis: insights from single-molecule approaches. *Annu*
526   *Rev Biophys* **43**: 119–140.

527 25. Bustamante C, Cheng W, Mejia YX (2011) Revisiting the Central Dogma One
528   Molecule at a Time. *Cell* **144**: 480–497.

529 26. van Oijen AM, Dixon NE (2015) Probing molecular choreography through single-
530   molecule biochemistry. *Nat Struct Mol Biol* **22**: 948–952.

531 27. Yodh JG, Schlierf M, Ha T (2010) Insight into helicase mechanism and function
532   revealed through single-molecule approaches. *Q Rev Biophys* **43**: 185–217.

533 28. Frank J, Gonzalez RL (2010) Structure and dynamics of a processive Brownian motor:
534   the translating ribosome. *Annu Rev Biochem* **79**: 381–412.

535 29. Lerner E, Cordes T, Ingargiola A, Alhadid Y, Chung S, Michalet X, Weiss S (2018)
536   Toward dynamic structural biology: Two decades of single-molecule Förster resonance
537   energy transfer. *Science* **359**: eaan1133.

538 30. Cisse I, Okumus B, Joo C, Ha T (2007) Fueling protein DNA interactions inside porous
539   nanocontainers. *Proc Natl Acad Sci U S A* **104**: 12646–12650.

540 31. Swoboda M, Henig J, Cheng H-M, Brugger D, Haltrich D, Plumeré N, Schlierf M
541   (2012) Enzymatic oxygen scavenging for photostability without pH drop in single-
542   molecule experiments. *ACS Nano* **6**: 6364–6369.

543   32.   Cheng H-M, Gröger P, Hartmann A, Schlierf M (2015) Bacterial initiators form
544   dynamic filaments on single-stranded DNA monomer by monomer. *Nucleic Acids Res*
545   **43**: 396–405.

546   33.   Humphrey W, Dalke A, Schulten K (1996) VMD: visual molecular dynamics. *J Mol*
547   *Graph* **14**: 33–38, 27–28.

548   34.   van de Meent J-W, Bronson JE, Wiggins CH, Gonzalez RL (2014) Empirical Bayes
549   methods enable advanced population-level analyses of single-molecule FRET
550   experiments. *Biophys J* **106**: 1327–1337.

551   35.   Bonn F, Pantakani K, Shoukier M, Langer T, Mannan AU (2010) Functional
552   evaluation of paraplegin mutations by a yeast complementation assay. *Hum Mutat* **31**:
553   617–621.

554   36.   Mickler M, Hessling M, Ratzke C, Buchner J, Hugel T (2009) The large
555   conformational changes of Hsp90 are only weakly coupled to ATP hydrolysis. *Nat*
556   *Struct Mol Biol* **16**: 281–286.

557   37.   Ait-Haddou R, Herzog W (2003) Brownian ratchet models of molecular motors. *Cell*
558   *Biochem Biophys* **38**: 191–214.

559   38.   Astumian RD (1997) Thermodynamics and kinetics of a Brownian motor. *Science* **276**:
560   917–922.

561   39.   Aubin-Tam ME, Olivares AO, Sauer RT, Baker TA, Lang MJ (2011) Single-molecule
562   protein unfolding and translocation by an ATP-fueled proteolytic machine. *Cell* **145**:
563   257–267.

564   40.   Maillard RA, Chistol G, Sen M, Righini M, Tan J, Kaiser CM, Hodges C, Martin A,
565   Bustamante C (2011) ClpX(P) generates mechanical force to unfold and translocate its
566   protein substrates. *Cell* **145**: 459–469.

567   41.   Kenniston JA, Baker TA, Fernandez JM, Sauer RT (2003) Linkage between ATP
568   consumption and mechanical unfolding during the protein processing reactions of an
569   AAA+ degradation machine. *Cell* **114**: 511–520.

570   42.   Grieb MS, Nivina A, Cheeseman BL, Hartmann A, Mazel D, Schlierf M (2017)
571   Dynamic stepwise opening of integron attC DNA hairpins by SSB prevents toxicity
572   and ensures functionality. *Nucleic Acids Res* **45**: 10555–10563.

573

574 **Supplementary Information**

575

576 **ATPase and protease domain movements in the bacterial AAA+ protease**

577 **FtsH are driven by thermal fluctuations**

578

579 Martine Ruer[1,2,†], Georg Krainer[1,3,†], Philip Gröger[1], Michael Schlierf[1,*]

580

581 [1] B CUBE – Center for Molecular Bioengineering, Technische Universität Dresden,

582 Arnoldstr. 18, 01307 Dresden, Germany

583 [2] Current address: Max Planck Institute of Molecular Cell Biology and Genetics (MPI-CBG),

584 Pfotenhauer Str. 108, 01307 Dresden, Germany

585 [3] Molecular Biophysics, Technische Universität Kaiserslautern (TUK), Erwin-Schrödinger-

586 Str. 13, 67663 Kaiserslautern, Germany

587

588 [†] These authors contributed equally to this work.

589 [*] Corresponding author. Tel: +49 351 463 43050; E-mail: michael.schlierf@tu-dresden.de

590   **Supplementary Figures**

591
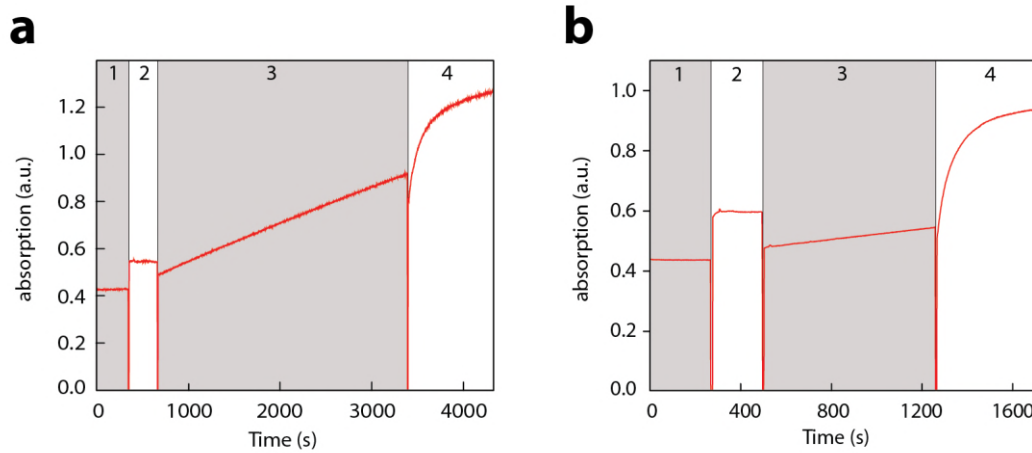
592

593   **Figure S1. ATPase activity assay of TmFtsH$_{184,513}$ (a) and TmFtsH$_{184,513}$-A359V (b).**
594   Monitored is the absorbance of 2-amino-6-mercapto-7-methyl-purine at 360 nm that is
595   generated in the EnzChek Phosphate Assay upon release of free phosphate in solution.
596   The four phases indicate (1) the background absorption of the buffer (20 mM HEPES
597   pH 8.0, 150 mM KCl, 10% glycerol, 5 mM MgOAc, 12.5 µM ZnOAc), (2) the
598   absorbance upon addition of 1 mM ATP, (3) the absorbance upon addition of 14.4 µM
599   TmFtsH$_{184,513}$ or TmFtsH$_{184,513}$-A359V, and (4) the absorbance upon addition of 0.8 µM
600   cI–ssrA substrate. The reactions were performed at room temperature.
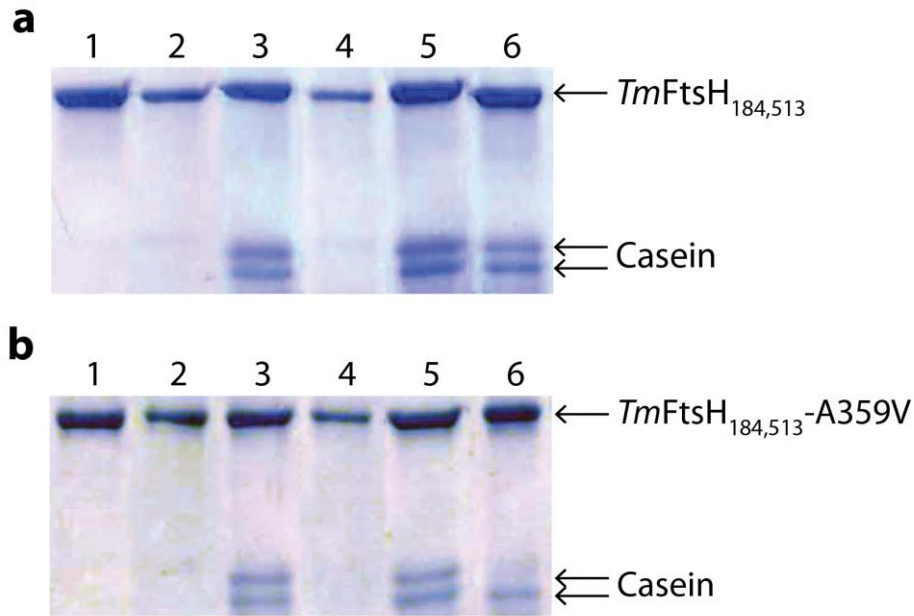
Figure S2. Protease activity of *Tm*FtsH$_{184,513}$ and *Tm*FtsH$_{184,513}$-A359V. a) *Tm*FtsH$_{184,513}$ (2.4 µM) incubated with 1 mM casein and 1 mM ATP at 24°C (1) and at 50°C (2); with 1 mM casein only at 24°C (3) and at 50°C (4); and with 1 mM casein, 1 mM ATP, and 0.1 mM EDTA at 24°C (5) and at 50°C (6). b) *Tm*FstH$_{184,513}$-A359V (2.4 µM) incubated with 1 mM casein and 1 mM ATP at 24°C (1) and at 50°C (2); with 1 mM casein only at 24°C (3) and at 50°C (4) and with 1 mM casein, 1 mM ATP, and 0.1 mM EDTA at 24°C (5) and at 50°C (6). The reaction was conducted overnight in buffer containing 20 mM HEPES pH 8.0, 150 mM KCl, 10% glycerol, 5 mM MgOAc, 12.5 µM ZnOAc.

611
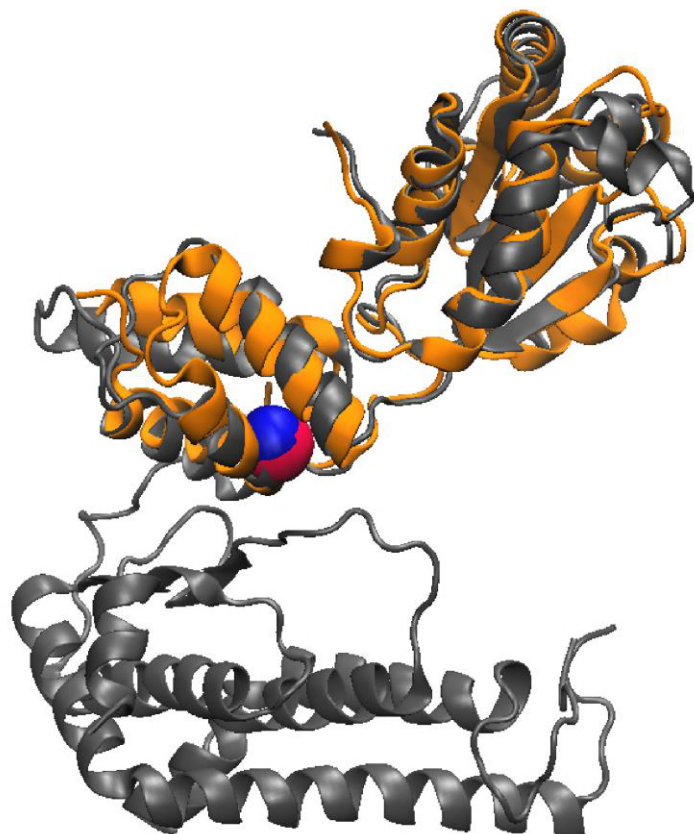
Figure S3. Structural alignment of *Tm*FtsH (gray; pdb: 3KDS) and its structural human homolog paraplegin (orange; pdb: 2QZ4). Alanine residue 359 (blue, C$_\alpha$) and the homologous pathogenic mutation A510V (red, C$_\alpha$) are highlighted. Both mutations are located at the boundary of the ATPase and protease domains. Alignment was performed in VMD.
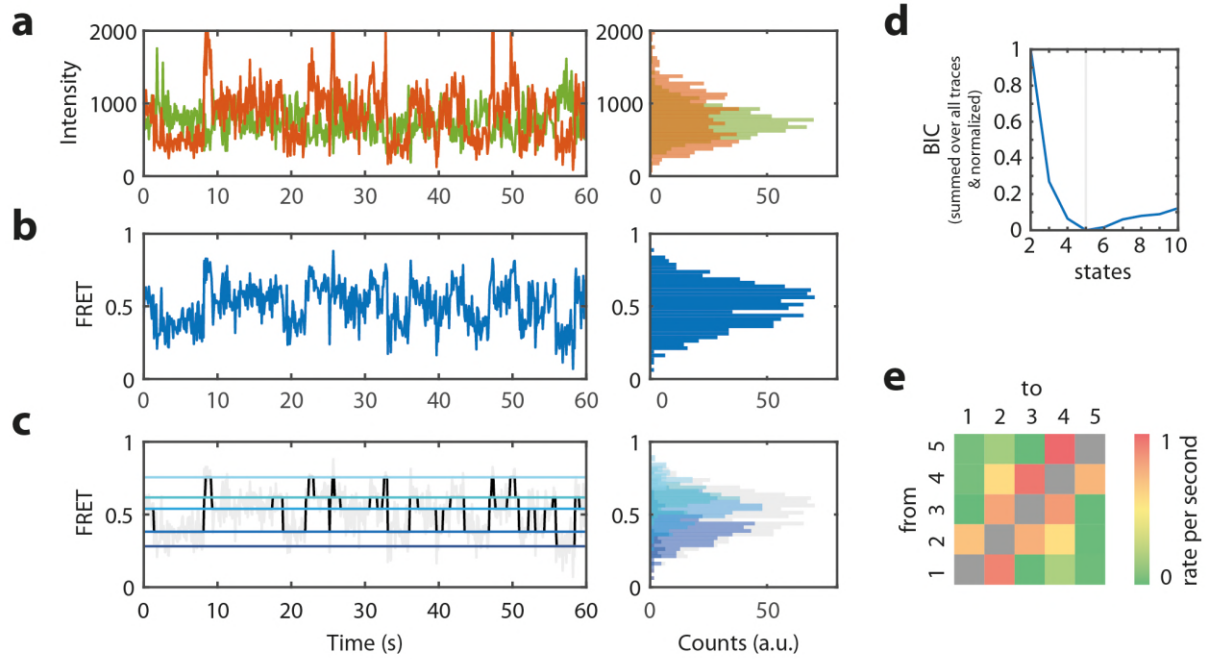
Figure S4. *Tm*FtsH$_{184,513}$ **with 1 mM ATP.** a) Representative donor and acceptor fluorescence intensity time trajectories (left panel) and their distributions (right panel). b) smFRET time trajectory (left panel) constructed from (a) and the derived FRET efficiency histogram (right panel) c) Viterbi path reconstruction of the smFRET time trajectory in (b) using a five-state model (left panel) and the derived histogram (right panel) d) Global BIC function. e) Heatmap of all conformational transition rates of *Tm*FtsH$_{184,513}$ in the presence of ATP.
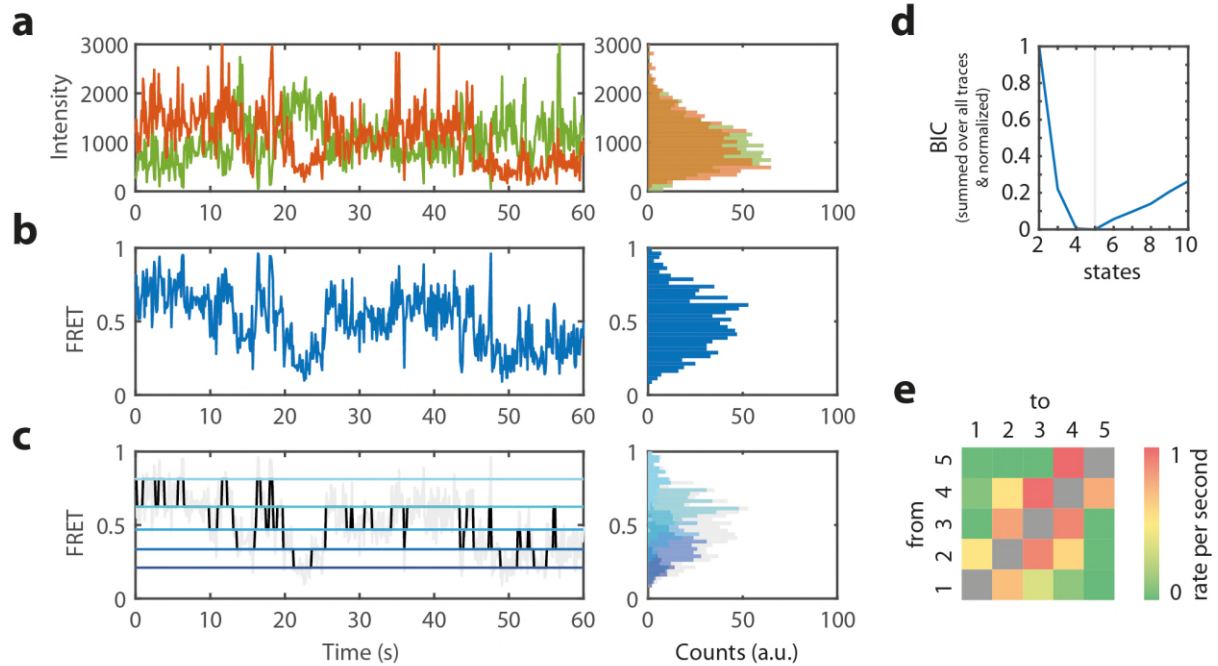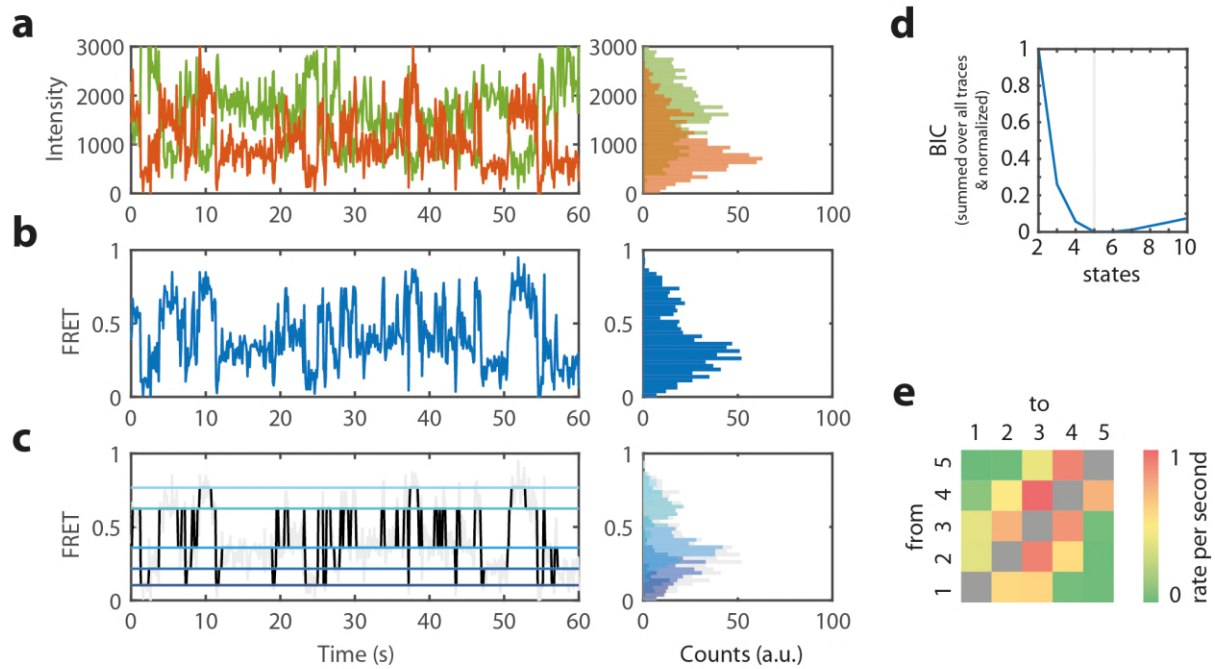
Figure S5. *Tm*FtsH$_{184,513}$-A359V without ATP. a) Representative donor and acceptor fluorescence intensity time trajectories (left panel) and their distributions (right panel). b) smFRET time trajectory (left panel) constructed from (a) and the derived FRET efficiency histogram (right panel) c) Viterbi path reconstruction of the smFRET time trajectory in (b) using a five-state model (left panel) and the derived histogram (right panel) d) Global BIC function. e) Heatmap of all conformational transition rates of *Tm*FtsH$_{184,513}$-A359V in the absence of ATP.

**Figure S6.** *Tm*FtsH$_{184,513}$-A359V with 1 mM ATP. a) Representative donor and acceptor fluorescence intensity time trajectories (left panel) and their distributions (right panel). b) smFRET time trajectory (left panel) constructed from (a) and the derived FRET efficiency histogram (right panel) c) Viterbi path reconstruction of the smFRET time trajectory in (b) using a five-state model (left panel) and the derived histogram (right panel) d) Global BIC function. e) Heatmap of all conformational transition rates of *Tm*FtsH$_{184,513}$-A359V in the presence of ATP.
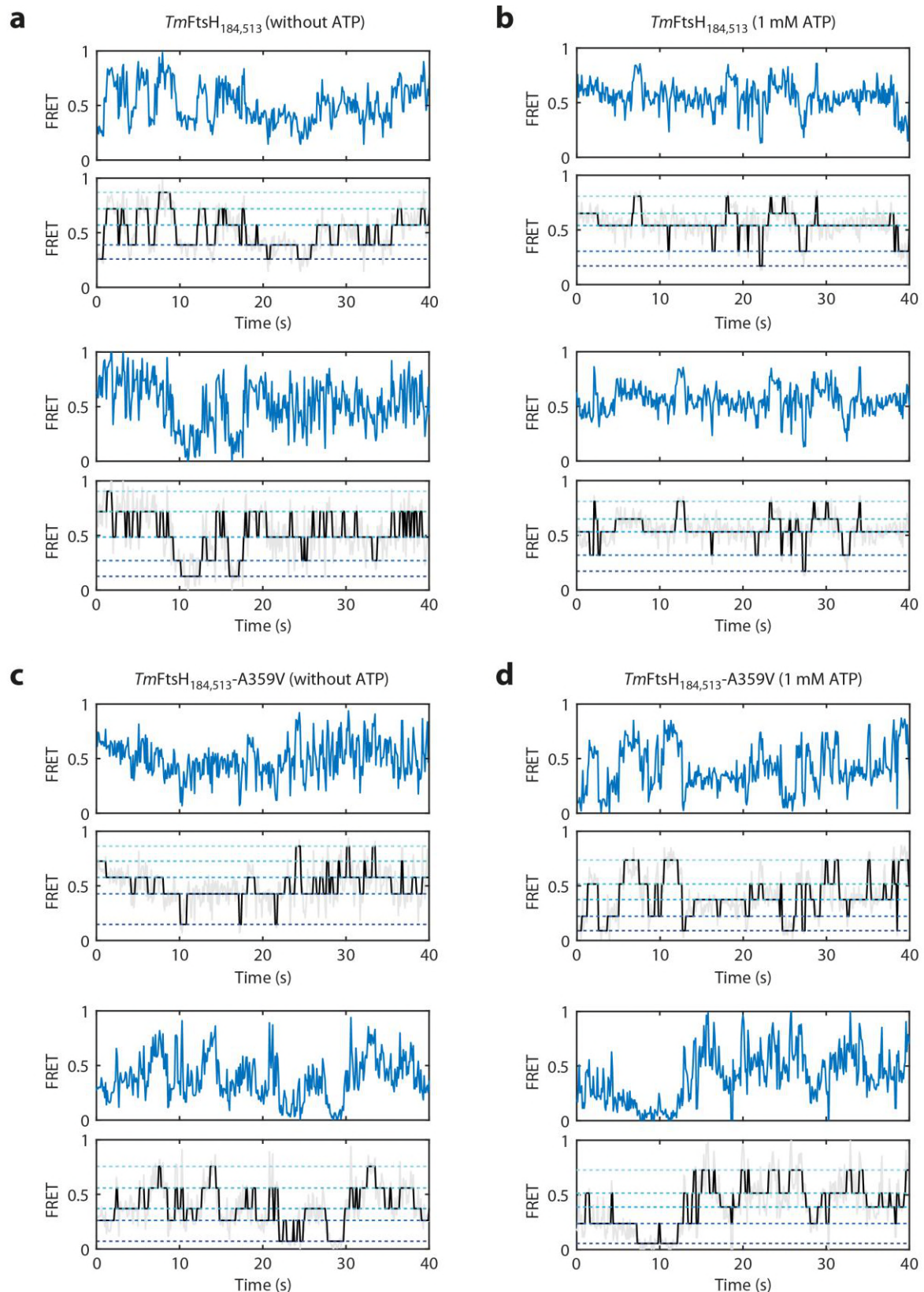
Figure S7. Selection of smFRET time trajectories of *Tm*FtsH$_{184,513}$ and *Tm*FtsH$_{184,513}$-A359V in the presence and absence of ATP. Top panels: smFRET time trajectories. Bottom panels: Viterbi path reconstruction of the smFRET trajectories using a five-state model.